Silicon (2024) 16:2621–2634
https://doi.org/10.1007/s12633-024-02847-7

RESEARCH

Study Attenuation Parameters and Physical Properties of Silicone Rubber Reinforced with Nano- and Micro-Sized Aluminum Oxide Composites

Ahmed M. El-Khatib[1] · E. Elesh[2] · Mohamed S. Hamada[3] · Eslam M. Sabry[2] · Mona M. Gouda[1]

Received: 29 October 2023 / Accepted: 7 January 2024 / Published online: 27 January 2024

Abstract
Theoretical and practical research has been done on reinforced polymer composites, a more recent type of improved shielding material. This study examined the protective qualities of silicone rubber packed with nano- and micro-sized Al_2O_3. Aspects like the effective atomic number, mean free path, linear attenuation coefficient, and mass attenuation coefficient are used to evaluate these shielding materials. In terms of weight percentage and size, Al_2O_3 particles have been used to reinforce silicone rubber. Energy dispersive X-ray spectroscopy, X-ray diffraction, UV visible spectrometer, thermal analysis, and Fourier transform infrared spectroscopy have been investigated. The results show that aluminum oxide nanoparticles have a more homogeneous distribution within the samples than micro aluminum oxide particles, which is due to the fact that nanoparticles have a very large surface area-to-volume ratio when compared to the same material in bulk. As a result, the sample containing 40% by weight of nano Al_2O_3 has the largest attenuation coefficient value and the lowest half value layer (HVL), tenth value layer (TVL), and mean free path (MFP) values. Finally, it can be concluded that the sample containing nano Al_2O_3 can be utilized to create an innovative and versatile silicone rubber material. This material holds great potential for the manufacturing of gloves and protective jackets, specifically designed for radiation and nuclear shielding applications.

Keywords Silicone rubber · Micro-aluminum oxide · Nano-aluminum oxide · Radiation Parameters

1 Introduction

The use of radiation in numerous parts of daily life is no longer something that people can deny [1]. This is due to the widespread usage of radioactive gamma sources in healthcare, agriculture, industry, scientific research, and many other practical sectors [2]. Living organisms that depend on gamma energy face significant risks when exposed to gamma beams [3]. Due to the dangerous effects of these poisonous radiations being emitted by undetected radioactive sources, a helpful material as a barrier is always essential to saving lives, as are diverse materials. This shield's primary function is to reduce the potentially harmful dose by interacting with both the radiation source and its waning intensity [4]. For this purpose, large atomic number compounds like Pb blocks and metal-infused concrete are typically utilized. Other metal-based protective materials, such as copper, tungsten, and bismuth, are currently being employed [5]. Pb stands out from all of these materials due to its high atomic weight, low cost, and excellent density [6]. However, Pb exhibits several fundamental flaws that restrict its uses and applications, including its large weight, high toxicity, rigidity, and poor chemical stability.

Aluminum is known for its exceptional resistance to radiation damage, surpassing that of commonly used spacecraft materials by a factor of 100. Its lightweight nature and impressive strength-to-weight ratio have made it a staple in space hardware, serving as both a radiation shield and a structural enclosure. To combat radiation particles, current spacecraft employ multiple layers of thin aluminum shields with air gaps in between, effectively slowing down

✉ Mona M. Gouda
mona.mgouda@alexu.edu.eg

1 Physics Department, Faculty of Science, Alexandria University, Alexandria 21511, Egypt

2 Physics Department, Faculty of Science, Port Said University, Port Said 42522, Egypt

3 Experimental Nuclear Physics Department, Nuclear Research Center, Egyptian Atomic Energy Authority, Cairo 13759, Egypt

their impact. Furthermore, aluminum plays a crucial role in the construction of outer spacesuits, safeguarding astronauts from the harmful effects of radiation in the vastness of space. Notably, aluminum radiation shielding is also utilized in the production of nuclear protection suits. In the medical field, there is a growing interest in the utilization of personalized 3D-printed aluminum radiation shields [7]. These shields aim to minimize the toxicity experienced by normal tissues while simultaneously delivering a substantial radiation dose to cancer cells during radiation therapy. This innovative approach holds great promise for enhancing the effectiveness of cancer treatment while reducing the potential harm to healthy tissues [8].

Studying novel materials to shield people from radiation and reduce environmental contaminants is crucial and exciting. The attenuation of gamma beams by polymeric materials is a current area of research that is interesting [5, 9]. Polymer composites were extensively researched as substitute radiation-protective materials to get over these restrictions [10]. Polymers are helpful because of their flexibility in applications that call for a certain quality despite having very poor mechanical qualities. Under extreme strain conditions, they typically deform [11, 12]. Our understanding of the relationship between the structure of the polymers and their properties has supplemented the major advancements in polymer research during the last few years [13, 14]. Because of their desirable qualities, including durability, transparency, flexibility, ease of synthesis, and capacity to produce electrical and thermal resistance, polymers are the perfect materials for a wide range of industrial applications [15]. Many scientists are interested in the potential uses of polymer composites doped with fillers of high atomic number (Z) metals or metal oxides, such as tungsten (W), barium (Ba), lead (Pb), tin (Sn), gadolinium (Gd), and bismuth (Bi). Considering their special qualities [16, 17], which include affordable price, simplicity of processing, light weight, flexibility, good mechanical strength, and optical and electrical properties [18]. In industrial applications including waveguiding layers, biochemical sensor implantation, and extruding machines, the mechanical properties of polymers like stiffness and tensile strength are crucial [19–21].

Liquid silicone rubber is a thermoset polymer that cannot be remolded. It is commonly used as a filler material for radiation protection, particularly when combined with a high Z material. The backbone, or "main chain," of silicone rubber is composed of siloxane bonds (-Si–O-Si-). These bonds are known for their exceptional stability. The filler is utilized to enhance the attenuation properties of the composites. Various fillers and polymers were employed to create a reinforced polymer composite. Previous research has explored the use of nano- and micro-particle reinforced composites as shields against gamma rays and neutron flux. Silicone rubber stands apart from other elastomers due to the remarkable strength of the siloxane bond. While carbon bonds possess a binding energy of 355 kJ/mol, the siloxane bond boasts an impressive strength of 433 kJ/mol. This inherent characteristic grants silicone rubber superior heat resistance, exceptional chemical stability, and outstanding electrical insulation properties. Gouda M. M. et al. [10] demonstrated that the radiation protection properties of silicon rubber composites are influenced by the particle size and weight fraction of tin oxide. The effectiveness of shielding protection was assessed by measuring the linear attenuation coefficient and calculating the buildup factor. The results obtained from scanning electron microscopy (SEM) morphology images revealed that nanocomposites exhibit a more uniform distribution compared to microcomposites. Moreover, the shielding parameters of nanotin oxide composites were found to be superior to those of microtin oxide composites at equivalent weight fractions. Additionally, it was observed that as the concentration of tin oxide increased, the attenuation parameter also increased. In a study conducted by Rammah et al. [22], the radiation protection properties of silicate glasses reinforced with tin (II) oxide were examined. The researchers discovered that the shielding characteristics of the samples improved as the weight percentage of tin (II) oxide increased. Alavian et al. [23] investigated the shielding properties of light-density polyethylene (LDPE) filled with tungsten (W) of varying sizes and weight fractions. Their findings revealed that the weight fraction of W had a greater impact on attenuation properties compared to the size scale of W.

In this study, we utilized silicone rubber (polydimethylsiloxane) as a polymer matrix to investigate the impact of incorporating micro and nano Al_2O_3 as a filler. Our objective was to examine the changes in the linear attenuation coefficient, mass attenuation coefficient, half-value layer, and tenth-value layer.

2 Experimental Technique

2.1 Synthesis of Bulk and Nano Aluminum Oxide

Using an arc discharge method, bulk and nano aluminum oxide were created. The system is made up of the following parts:

(1) Manual metal arc (MMA) inverter DC welding equipment (CT33102 CROWN) with power supply for vaporizing aluminum metal.
(2) A cooling system that maintains a temperature of 10° C during the preparation.
(3) high-quality 99.99 percent aluminum electrodes as a cylindrical anode and cathode.

(4) Ethanol, where the aluminum electrodes are submerged on top of it and an electric arc discharge takes place inside of it [24].

A DC power source with a low voltage of 80 V and a high current of 20A was used to progressively advance the anode electrode toward the cathode electrode. Table 1 shows the parameters used in the fabrication of Al_2O_3. The aluminum electrode poles melted or evaporated as they came into contact because the two electrodes generated an arc discharge. These electrodes were placed 8 cm into ethanol, spaced approximately 1 mm apart, and vertically oriented at a roughly 70-degree angle. The ability of the metal electrode holders to swivel forward and backward during the arc discharge allowed for the best possible adjustment of the electrode gap.

The technique didn't involve the use of any chemical substances [25, 26]. The media employed was pure solutions (ethanol). The formation of nanoparticles from vaporized Al metal takes place in three stages: nucleation, cluster development, and condensing in ethanol. The bulk particles were obtained by transferring the ethanol to another container while keeping the bulk particles in the first container and using filtration paper to obtain them. The bulk particles were suspended in the ethanol along with the nano aluminum oxide that was concentrated under the container. By utilizing filtration sheets, it is possible to acquire the suspended nanoparticles.

2.2 Fabrication of Silicone Rubber / Al_2O_3 Composites

In this particular study, we utilized Al_2O_3 as a filler in both nano and micro sizes. We prepared free silicon rubber, as well as micro- and nanocomposites, with 10%, 20%, 30%, and 40% weight concentrations of aluminum oxide filler. To ensure a uniform mixture, the mixing process lasted for 15 min. Through catalyzed cross-linking reactions, silicon is converted into an elastomeric solid structure. Approximately 2 wt% of a stiffener is added to the polymer liquid.

Table 1 Parameters used in the fabrication of Al_2O_3

Key parameters	Value
Values Discharging voltage (average value)	80 V
Discharging current (average values)	30 A
cathode disk (length, diameter)	10 cm, 5 mm
Anode (length, diameter)	8 cm, 4 mm
The temperature of the solution (before & after)	10 °C
Volume of solution	2 L
Pressure	Atmospheric
Discharging Duration time	30 min

In order to eliminate air bubbles from the matrix, a vacuum was applied for a duration of 30 min.The homogeneous mixture is molded into cylinders with a diameter of 3 cm and varying thicknesses. After a waiting period of 24 h, the mixture transforms into a solid elastomeric material. The Archimedes technique was employed to determine the average density (g/cm^3) of all the samples, using water as the immersion medium.

2.3 Characterization Techniques

X-ray diffraction (XRD) was carried out using a Bruker Diffractometer (D8 DISCOVER,USA) Diffractometer and Cu-K radiation with a wavelength of 1.54060 Angstrom at the laboratory of Alexandria University, Alexandria, Egypt, to determine the structural properties. Fourier transform infrared spectroscopy of nano and bulk Al_2O_3 was carried out in the 500 – 4000 cm^{-1} spectral range using an ATI Mattson (Infinity series FT-IR, India) spectrophotometer. Free silicone rubber, micro and nano aluminum oxide /silicone rubber were examined for morphology using a JEOL-scanning electron microscopy (JXA810, England).Transmission electron microscope (TEM) [JEM-2100F, JEOL, Japan], operating at 200 kV, has been employed in our experimental research) at the Nawah Laboratory in Cairo, Egypt. The samples receive an Au coating thanks to ion sputter coating technology. Thermal analysis was performed for bulk and nano Al_2O_3 to determine the thermal stability of the materials using the (NEXTA DSC, Japan) instrument.

2.4 Setup for Gamma-ray Spectroscopy

The gamma-radiation tests used five typical radioactive point sources from the Physikalisch-Technische Bundesanstalt PTB in Braunschweig and Berlin: ^{241}Am, ^{133}Ba, ^{137}Cs, ^{60}Co, and ^{152}Eu, emitting energies between 59.53 keV and 1408.01 keV [27]. Table 2 shows the photon energies and Half-life time for the used radioactive sources. By using the radiation physics laboratory at Alexandria University in Egypt and the Canberra Type 802 scintillation detector, measurements of the gamma-ray shielding properties of the micro- and nanocomposites were made [28]. A photomultiplier tube, a 14-pin connector, and a NaI(Tl) crystal with dimensions of 76.2 in height and 38.1 mm in radius make up the detector, which has a highly efficient and resolution of 8.5% at 661 keV [29]. Typical operating voltages are + 110 V dc from the cathode to the anode and + 80 V dc from the dynode to the dynode [30].

Emerging photons from the sample under examination interacted with the detector, which transformed them into electrical signals of various sizes and presented them as peaks in a spectrum using the Genie 2000 software [31]. After doing each measurement a sufficient number of times,

Table 2 Photon energies and Half-life time for the used radioactive sources

Radioactive source	Photon Energy (keV)	Half-Life ($T_{1/2}$ Days)
^{241} Am	59.51	157,680
^{60}Co	1173.2	1925.31
	1332.5	
^{137}Cs	661.66	11,004.98
^{133}Ba	80.99	3847.91
	356.01	
^{152}Eu	121.782	4943.29
	244.697	
	778.905	
	964.079	
	1408.013	

the gamma spectra were captured, ensuring that the statistical error would be less than 1% [32]. The net area under each spectrum peak was then entered into an Excel sheet for each energy and thickness to calculate the shielding properties of the examined composites [33]. To ensure the experiment's validity, the experimental attenuation coefficient values were compared to those from the XCOM program.

2.5 Radiation Parameters

The chance of photons interacting with matter per unit length is the linear attenuation coefficient (μ), or LAC (cm^{-1}), and it is calculated empirically using the well-known Beer-Lambert's law [34].

$$\mu = -\frac{1}{x} Ln\frac{I}{I_0} \tag{1}$$

where x is the target material's thickness, and I and I_0 are the transmitted and incident intensities, respectively. It should be noted that the mass attenuation coefficient, or MAC (μ/ρ), can be calculated by dividing the sample's empirical linear attenuation coefficient (μ) by its density (ρ) [35].

$$MAC = \frac{\mu}{\rho} \tag{2}$$

MACs were theoretically estimated using the NIST XCOM web program [36] to verify the authenticity of the experimental data. It is beneficial to extend the calculations to include the other shielding parameters for the examined samples, the half value layer (HVL), the tenth value layer (TVL), and the mean free path (MFP) [37]. According to the following relations, the HVL and TVL are determined as the thicknesses needed to reduce the incident photon intensity by a factor of 1/2 and 1/10, respectively [38].

$$HVL = \frac{Ln2}{\mu} \tag{3}$$

$$TVL = \frac{Ln10}{\mu} \tag{4}$$

The average distance a photon travels inside the sample without encountering any interactions is known as the MFP (cm) [39].

$$MFP = \frac{1}{\mu} \tag{5}$$

The shielding capabilities of composites are described by the effective atomic number (Z_{eff}) parameter [40]. Gamma-ray energy and the characteristics of pure elements play a role [41].

$$Z_{eff} = \frac{\sum_i W_i A_i \left[\frac{\mu}{\rho}\right]_i}{\sum_i W_i \frac{A_i}{Z_i} \left[\frac{\mu}{\rho}\right]_i} \tag{6}$$

where W_i, A_i, and Z_i are, respectively, the weight percentage, atomic weight, and element i in the composite.

The relative deviations for the measured mass attenuation coefficient compared to the XCOM result (Δ_1) and between micro and nano measured results (Δ_2) are given by the following equations:

$$\Delta_1\% = \frac{XCOM - EXP}{EXP} X100 \tag{7}$$

$$\Delta_2\% = \frac{Nano - Micro_{Exp}}{Micro_{Exp}} X100 \tag{8}$$

3 Results and Discussion

3.1 The Characterization

Energy dispersive X-ray spectroscopy (Edx) is used to characterize element compositions of bulk aluminum oxide, as shown in Fig. 1. The EDX can show the percentage of elements in a sample. As shown graphically, there is a large percentage of aluminum (Al) in the MICRO sample, followed by oxygen (O). It mesured at the laboratory of Alexandria University, Alexandria, Egypt.

The XRD spectrum of nano Al_2O_3 is shown in Fig. 2. It shows the phase analysis in the 2Θ range between 5° and 80°. The spectrum gave rise to the major Al_2O_3 at 2Θ peaks. To ascertain the structural characteristics, XRD was performed with a wavelength of 1.54060 Angstrom.

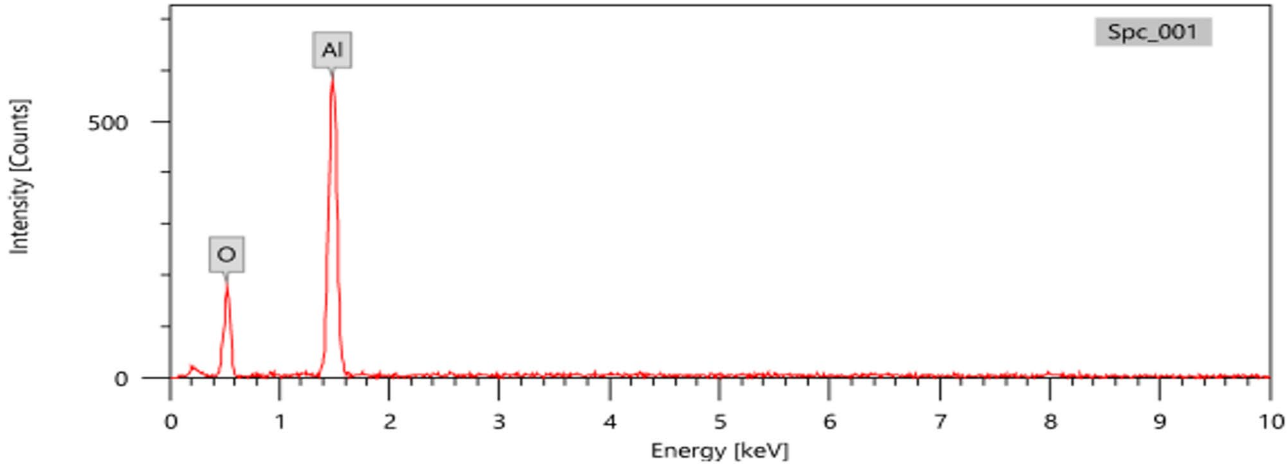

Items	Value
measurement conditions	
Acceleration voltage	20.00 kV
Probe current	-
Magnification	x 1200
Process time	T2
Measurement detector	First
Live time	30.00 seconds
Real time	30.04 seconds
Dead time	0.00 %
Count rate	346.00 CPS

Display name	Standard data	Quantification method	Result Type
Spc_001	Standardless	ZAF	Oxide (Number of oxygen 24)

Chemical formula	Line	Mass%	Mol%	Cations
O	K			
Al2O3	K	100.00±2.03	100.00±2.03	16.00
Total		100.00	100.00	
Spc_001				Fitting ratio 0.1706

Fig. 1 EDX analysis of bulk aluminum oxide

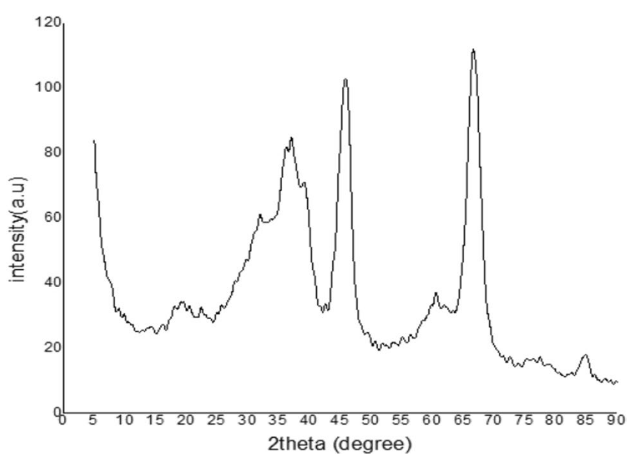

Fig. 2 XRD for a sample of Al_2O_3

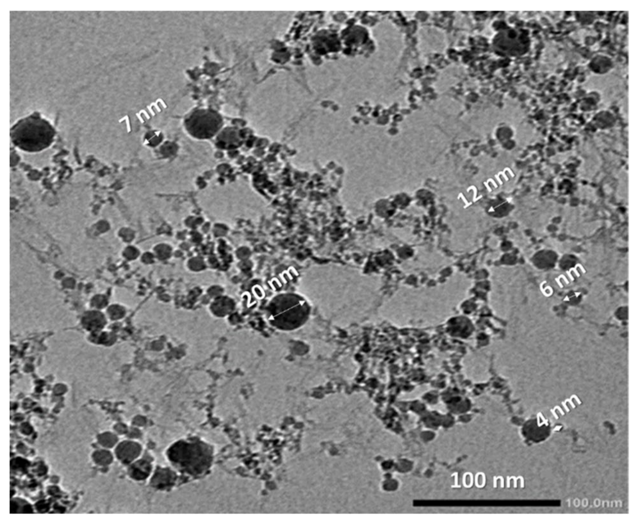

Fig. 3 TEM images of nano-aluminum oxide particles

The particle size of nano aluminum oxide was estimated using a Transmission Electron Microscope (TEM) [JEM-2100F, JEOL, Japan] operating at 200 kV, at the laboratory of Alexandria University, Alexandria, Egypt, as depicted in Fig. 3. The nanoparticles are composed of networked spherical particles with a size ranging from 4 to 20 nm and their average was found to be around 10 nm, with a standard deviation of 5%. These nanoparticles are connected through nanowires with a very thin diameter of 2–3 nm. The growth mechanism of the mixed nanoparticles and nanowires of Al_2O_3 through the arc discharge process includes both nucleation and growth stages of the vapor–liquid-solid (VLS) process [42]. The nanoparticles may be started with the dissolution of gaseous sources into a few nanometer-sized liquid droplets, followed by the nucleation and growth of the crystalline nanoparticles [43] and the nanowires are grown from the accumulated nanoparticles. The larger nanoparticles of 12–20 nm are those in which a dense amount of the smaller accumulated nanoparticles are combined.

Aluminum oxide/silicone rubber composites and free silicone rubber were characterized using the scanning electron microscope. The images show how Nanoparticles are arranged and shaped within the composite, demonstrating how carefully the particles and material were prepared The silicone rubber cross-section morphology was found to be smooth and transparent in comparison to filled composites in Fig. 4, which shows the SEM of free silicone rubber, 40% micro aluminum oxide/silicone rubber, and 40% nano aluminum oxide/silicone rubber. Bulk Alumina particles are agglomerated with sizes of about 5–25 µm are randomly dispersed in the silicone rubber matrix as pointed in Fig. 4b with red circles. While agglomerated particles of sizes range from 1–3 µm (red circles in Fig. 4c) and nanoparticles are thoroughly well dispensed in the silicone rubber matric as pointed in Fig. 4c (yellow arrows). Due to the homogenous distribution of nano aluminum oxide particles compared to micro aluminum oxide particles within the silicone rubber sample, the nano combination offered high protective performance. Also, SEM is used to determine the size of bulk aluminum oxide, which was found to be 25 µm with a standard deviation of 2.68 µm.

UV/Visible Spectrophotometer Jenway 6305 and a Xenon lamp were used with a range of wavelengths of 198 to 1000 nm, the UV characterization determines the attenuation of light passing through a substance (scatter plus absorption) [44]. According to Fig. 5, which displays the UV–visible spectra for two samples of nano Al_2O_3, it is evident that the first sample, with a concentration of 1 mg/ml, exhibits a higher optical density compared to the second sample, which is diluted four times from the first. Consequently, the sample with a higher concentration demonstrates greater absorption. Notably, the highest absorption value is observed at a wavelength of 250 nm. UV/visible characterization was done at the laboratory in Alexandria, Egypt.

Fourier transform infrared spectroscopy (FT-IR (data analysis can show whether nanofiller is present in a polymer matrix and how they interact with one another. Selecting the

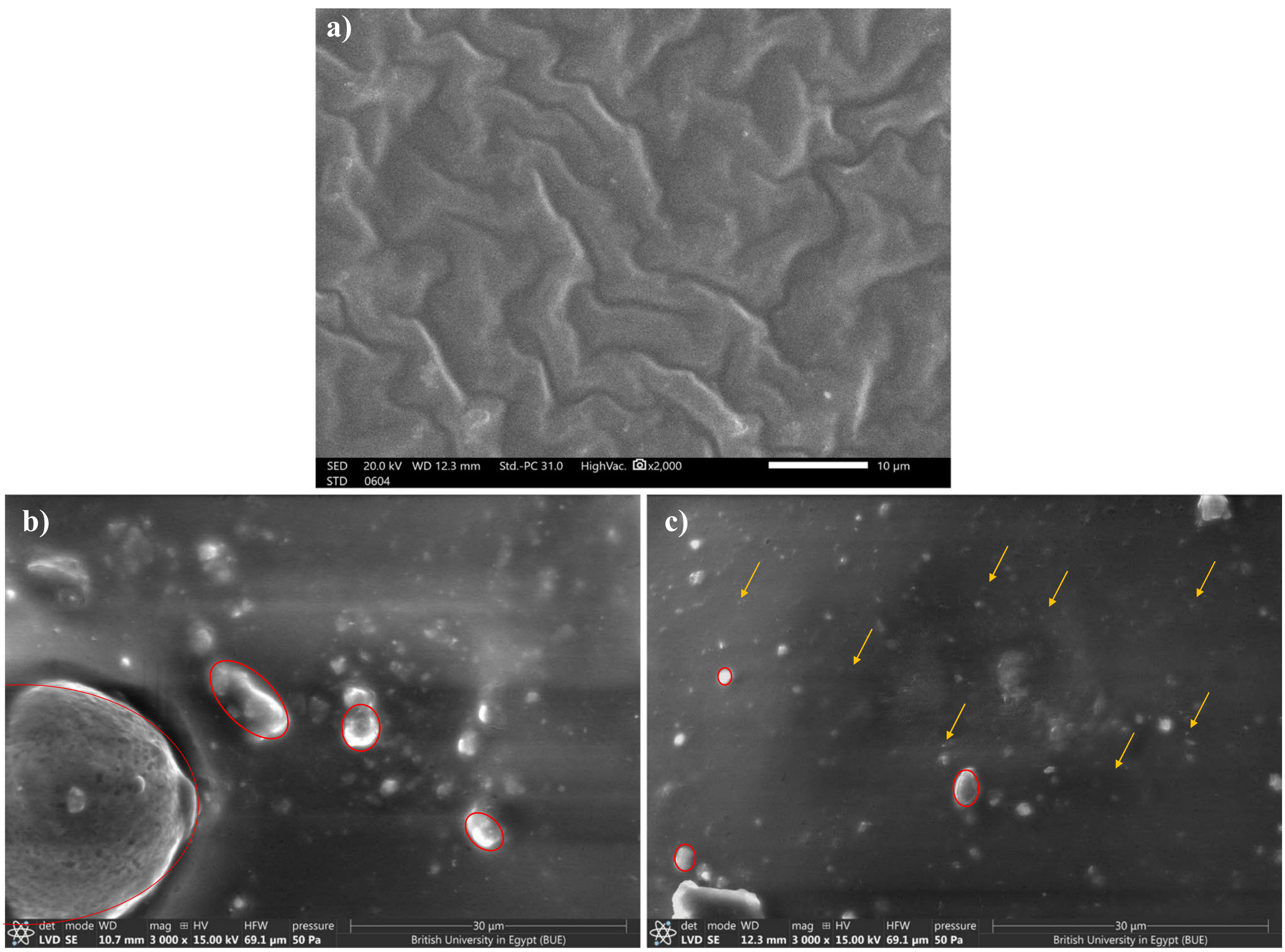

Fig. 4 SEM image of (**a**) free silicone rubber, (**b**) 40% micro aluminum oxide /silicone rubber, and (**c**) 40% nano aluminum oxide/ silicone rubber

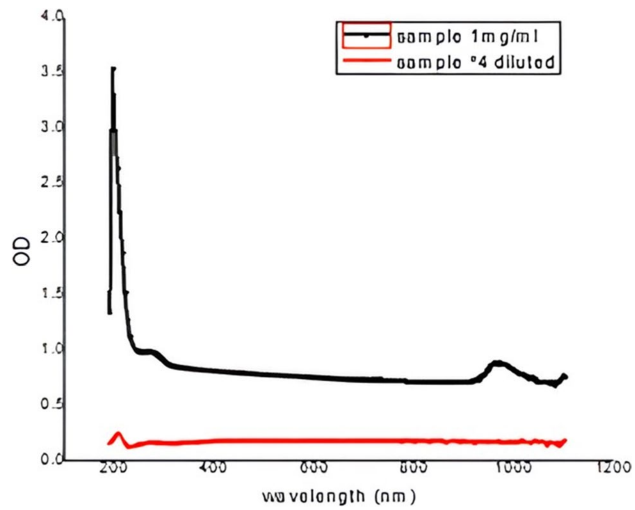

Fig. 5 UV is visible for two samples of nano Al_2O_3 the first sample with a concentration of 1 mg/ml and the second sample is diluted four times from the first sample

right IR sources is crucial to get the best IR spectra of the samples. FTIR was performed for bulk Aluminum and nano Aluminum oxide at Nawah Laboratory in Cairo, Egypt, as shown in Fig. 6. The FTIR spectrum of micro-aluminum oxide (Fig. 6) showed a sharp peak at 2963 cm^{-1} attributed to the -OH stretching vibrations related to the lattice of water molecules; this may indicate the presence of moisture in the powder. A weak band appears at 1408 cm^{-1} associated with Al–OH bond stretching also, a strong peak at 1258 cm^{-1} due to Al-O bond vibration. In addition, the available bands at 1009, 787, 700, and 463 cm^{-1} were the consequence of the bending vibrations of the Al–O–Al group. The same observations were reported for the nanosize of alumina in Fig. 6, in addition to the appearance of the peak at 3662 cm^{-1} that related to the OH vibrational group for alcohol, indicating the presence of ethanol due to preparation. the nano Al_2O_3 spectrum resembles that of the bulk form rather closely, suggesting that the chemical structure of the studied sample doesn't change [45, 46]. The rising intensities of peaks for nano Al_2O_3 indicate a decrease in crystallite sizes in nano form [46].

The thermal behavior of bulk Al_2O_3 and nanoparticles Al_2O_3 are depicted in Figs. 7 and 8, respectively, showing curves of DTA (Differential Thermal Analysis), TGA (Thermogravimetric Analysis), and DrTGA (The derivative thermogravimetric analysis). It can be observed in Fig. 7 that bulk Al_2O_3 allows the separation of two decomposition steps. The first decomposition step (TGA curve) was a slow and gradual weight loss of 5.25% at 33.39 – 307.09 °C, which corresponds to one weak endothermic peak in the DTA curve. The second decomposition step (TGA curve) at 308.93 – 595.99 °C is assigned a dramatic mass loss of 57.96%, corresponding to three exothermic peaks in the DTA curve. Concerning Al_2O_3 nanoparticles, Fig. 8 shows that the first decomposition step at 34.37 – 258.82 °C with

Fig. 6 FTIR for bulk and nano Aluminum oxide

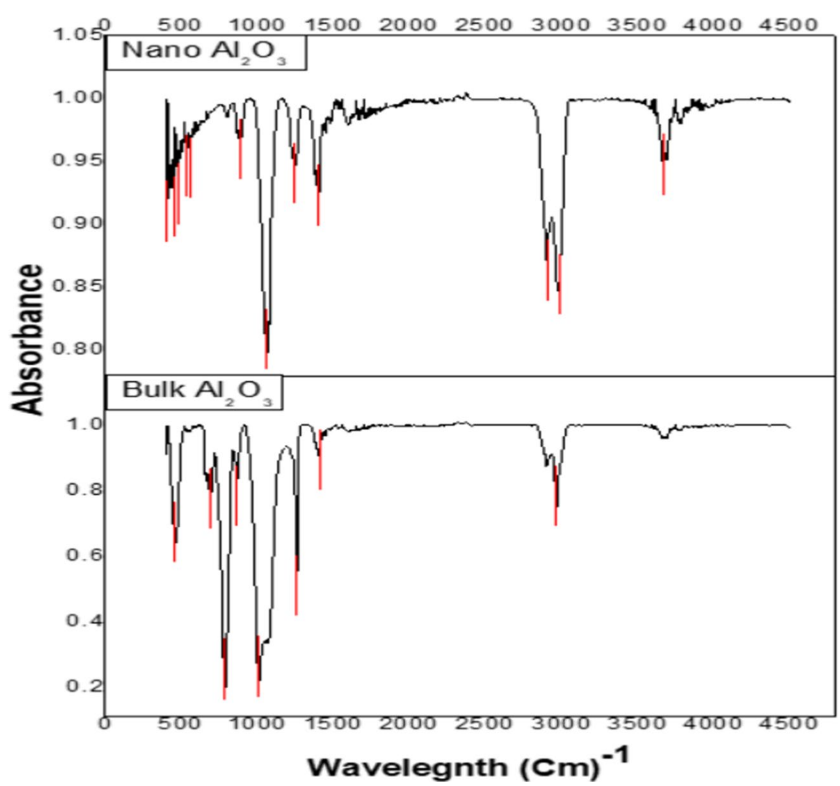

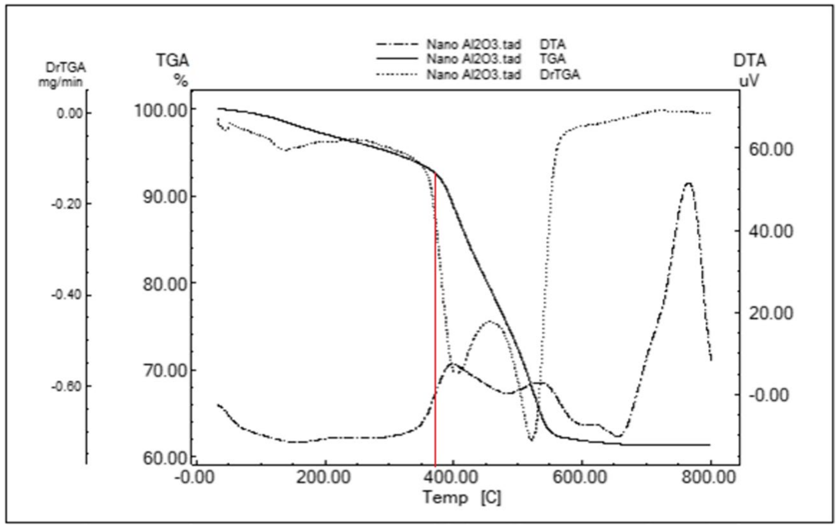

Fig. 7 Thermal analysis for 40% micro aluminum oxide

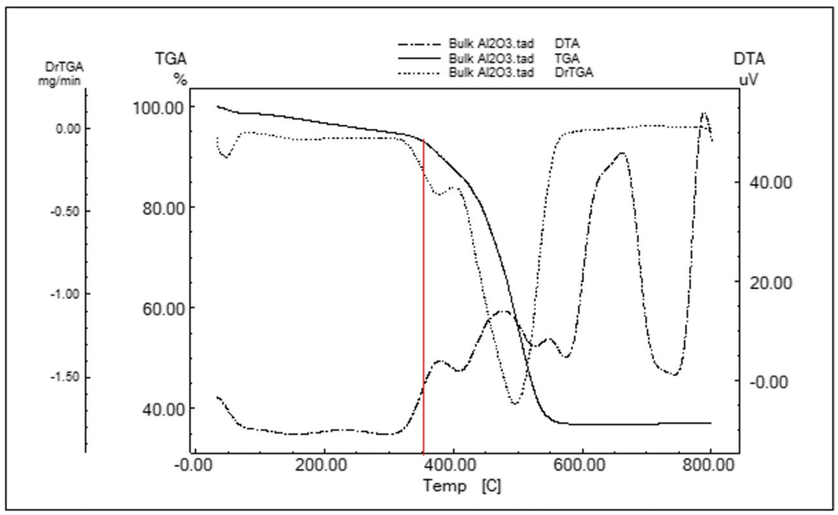

Fig. 8 Thermal analysis for 40% nano aluminum oxide

a mass loss of 4.076% corresponds to one weak endothermic peak. The mass loss accompanying this step could be attributed to the removal of moisture and water molecules embedded inside the material. The second decomposition is of exothermic nature (two peaks) with a mass loss of 34.56% at 260.21 – 679.16 °C that could be attributed to the phase transition. Here, the thermal degradation temperatures showed a close trend for bulk and nanoparticles of Al_2O_3, however, the depletion in the mass loss of the nanoparticles with ca. 23.4% could be regarded as the improved stability of Al_2O_3 nanoparticles. Generally, the higher the temperature corresponding to the decrease of the TG curve, the higher the temperature corresponding to the beginning of decomposition, the more stable the material is. The derivative thermogravimetric analysis (DrTGA) has also been used to describe the step ranges for better precision. The glass transition temperature (T_g) of bulk Al_2O_3 was 355 °C, but the T_g of nano Al_2O_3 was 365 °C. This indicates that the T_g for nano Al_2O_3 is higher than that of bulk Al_2O_3. This phenomenon is attributed to the existence of nanoparticles, which function as physical cross-links, hence augmenting the matrix's stiffness. When the loading is higher and the nanoparticles are smaller, the T_g enhancement effect is more noticeable.

3.2 Gamma Rays Stydies

The experimental mass attenuation coefficient (MAC) of free silicone rubber, 10%,20%,30%, and 40% micro Al_2O_3/SR, and 40% nano Al_2O_3/SR against gamma rays in the 59.53–1408.01 keV range and the corresponding theoretical mass attenuation coefficient determined from XCOM are shown in Table 3. The relative deviation for free silicone rubber ranges from 1.86 to 3.5. For 10% micro Al_2O_3/SR, the range is from 0.6 to 3.26. For 20% micro Al_2O_3/SR, the range is from 0.93 to 2.83. For 30% micro Al_2O_3/SR, the

Table 3 Variation of mass attenuation coefficient (μ_m) with gamma-ray energies for free silicone rubber and (10%, 20%, 30%,40%) Micro Al_2O_3/SR

Sample name	Energy (keV)	Density (g/cm^3)	Mass attenuation coefficient μ_m(cm^2/g)		
			Measured	XCOM	Δ_1%
SR	59.53	1.15 ± 0.02	0.2316 ± 0.0012	0.2261	2.4108
	80.99		0.1880 ± 0.0050	0.1841	2.0886
	121.78		0.1591 ± 0.0021	0.1561	1.9272
	244.7		0.1260 ± 0.0011	0.1236	1.9721
	356.01		0.1105 ± 0.0002	0.1076	2.6524
	661.66		0.0863 ± 0.0001	0.08324	3.6216
	778.9		0.0791 ± 0.0001	0.07730	2.3338
	964.08		0.0712 ± 0.0021	0.06988	1.8568
	1173.24		0.0657 ± 0.0023	0.06343	3.5044
	1332.5		0.0614 ± 0.0004	0.05944	3.2981
	1408.01		0.0591 ± 0.0002	0.05779	2.3173
10% Micro Al_2O_3/SR	59.53	1.26 ± 0.01	0.2279 ± 0.0002	0.22480	3.2551
	80.99		0.1871 ± 0.0022	0.18270	2.3781
	121.78		0.1583 ± 0.0001	0.1547	2.3123
	244.7		0.1253 ± 0.0001	0.12240	2.3313
	356.01		0.1073 ± 0.0004	0.10670	0.6062
	661.66		0.0831 ± 0.0032	0.08248	0.7410
	778.9		0.0789 ± 0.0001	0.07660	3.0301
	964.08		0.0711 ± 0.0001	0.06924	2.7232
	1173.24		0.0639 ± 0.0002	0.06286	1.7539
	1332.5		0.0599 ± 0.0005	0.05890	1.7849
	1408.01		0.0585 ± 0.0002	0.05726	2.1974
20% Micro Al_2O_3/SR	59.53	1.34 ± 0.04	0.2278 ± 0.0001	0.22360	1.8464
	80.99		0.1854 ± 0.0062	0.18120	2.2719
	121.78		0.1573 ± 0.0001	0.15330	2.5922
	244.7		0.1244 ± 0.0001	0.12130	2.5532
	356.01		0.1067 ± 0.0001	0.10570	0.9363
	661.66		0.0829 ± 0.0003	0.08172	1.5242
	778.9		0.0781 ± 0.0022	0.07590	2.8325
	964.08		0.0706 ± 0.0002	0.06861	2.8372
	1173.24		0.0632 ± 0.0001	0.06228	1.5500
	1332.5		0.0592 ± 0.0021	0.05836	1.4624
	1408.01		0.0574 ± 0.0001	0.05674	1.2703
30% Micro Al_2O_3/SR	59.53	1.46 ± 0.03	0.2239 ± 0.0011	0.22230	0.7536
	80.99		0.1850 ± 0.0020	0.17980	2.8260
	121.78		0.1572 ± 0.0001	0.15190	3.3796
	244.7		0.1243 ± 0.0003	0.12020	3.3337
	356.01		0.1066 ± 0.0002	0.10470	1.7900
	661.66		0.0826 ± 0.0051	0.08096	2.0077
	778.9		0.0775 ± 0.0011	0.07519	2.9849
	964.08		0.0701 ± 0.0002	0.06797	3.0372
	1173.24		0.0617 ± 0.0002	0.06170	0.1416
	1332.5		0.0587 ± 0.0001	0.05782	1.6061
	1408.01		0.0569 ± 0.0001	0.05621	1.2611

Table 3 (continued)

Sample name	Energy (keV)	Density (g/cm^3)	Mass attenuation coefficient μ_m(cm^2/g)		
			Measured	XCOM	Δ_1%
40% Micro Al_2O_3/SR	59.53	1.53 ± 0.02	0.2233 ± 0.0004	0.22100	1.0285
	80.99		0.1833 ± 0.0001	0.17840	2.6721
	121.78		0.1550 ± 0.002	0.1506	2.8734
	244.7		0.1226 ± 0.0022	0.11910	2.9172
	356.01		0.1059 ± 0.0002	0.10370	2.1372
	661.66		0.0817 ± 0.0003	0.08021	1.9246
	778.9		0.0762 ± 0.0021	0.07449	2.3013
	964.08		0.0685 ± 0.0001	0.06734	1.6930
	1173.24		0.0617 ± 0.0001	0.06112	1.0165
	1332.5		0.0573 ± 0.0002	0.05729	0.1482
	1408.01		0.0558 ± 0.0002	0.05569	0.2691

range is from 0.14 to 3.37. For 40% micro Al_2O_3/SR, the range is from 0.14 to 2.91. Lastly, for 40% nano Al_2O_3/SR, the range is from 2.8 to 15.7. All experimental results for free silicone rubber, 10%,20%,30%, and 40% micro Al_2O_3/SR are in good agreement with theoretical XCOM values. The mass attenuation coefficient decreases as the photon energy increases, while it increases with the increasing presence of Al_2O_3 in the sample. Notably, the sample's mass attenuation coefficient exhibits a significant value at a photon energy of 0.05953 MeV, gradually declining as the photon energy increases. This behavior can be attributed to the photon's partial interaction process. At lower photon energies, such as 0.05953 MeV, the attenuation values align with the photoelectric absorption, which is inversely proportional to E^3. In the intermediate energy range, Compton scattering becomes the dominant attenuation process, with attenuation being inversely proportional to E. For energies equal to or higher than 1.022 MeV, the mass attenuation values remain relatively constant due to the prevalence of the pair production process in this region [47–49].

According to the findings presented in Tables 3 and 4, the density of silicone rubber composites demonstrates a direct correlation with the percentage of aluminum oxide incorporated into the composites. Furthermore, it is worth noting that composites filled with nanoparticles exhibit a higher density when compared to those filled with microparticles at an equivalent weight fraction. Consequently, the utilization of nanocomposites yields superior shielding properties

Table 4 Variation of mass attenuation coefficient (μ_m) with gamma-ray energies for 40% Nano Al_2O_3/SR

Energy (keV)	Density (g/cm^3)	Measuread mass attenuation coefficient μ_m(cm^2/g)	Δ_2%
59.53	1.66 ± 0.02	0.2584 ± 0.0004	15.7188
80.99		0.2076 ± 0.0011	13.2570
121.78		0.1745 ± 0.0002	12.5806
244.7		0.1354 ± 0.0003	10.4405
356.01		0.1156 ± 0.0002	9.1596
661.66		0.0884 ± 0.0001	8.2007
778.9		0.0822 ± 0.0001	7.8740
964.08		0.0723 ± 0.0003	5.5474
1173.24		0.0651 ± 0.0016	5.5105
1332.5		0.0593 ± 0.0002	3.4904
1408.01		0.0574 ± 0.0002	2.8674

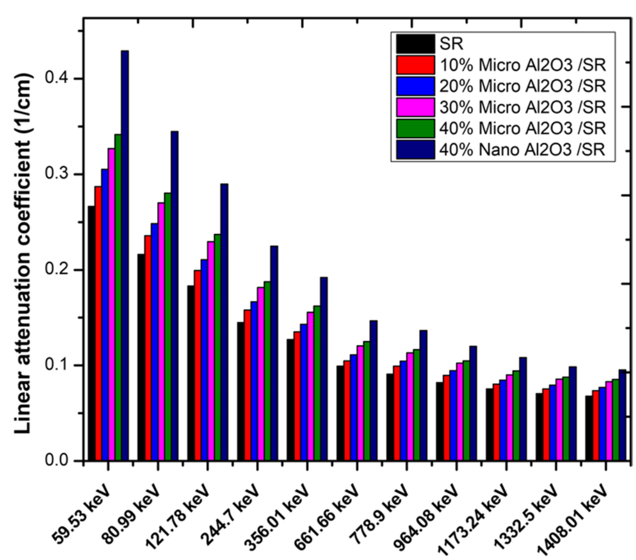

Fig. 9 The linear attenuation coefficients as a function of photon energy

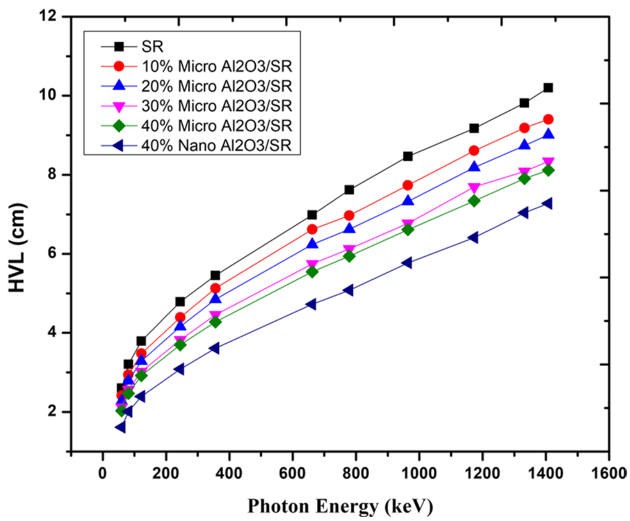

Fig. 10 The variation of the HVL as a function of photon energy

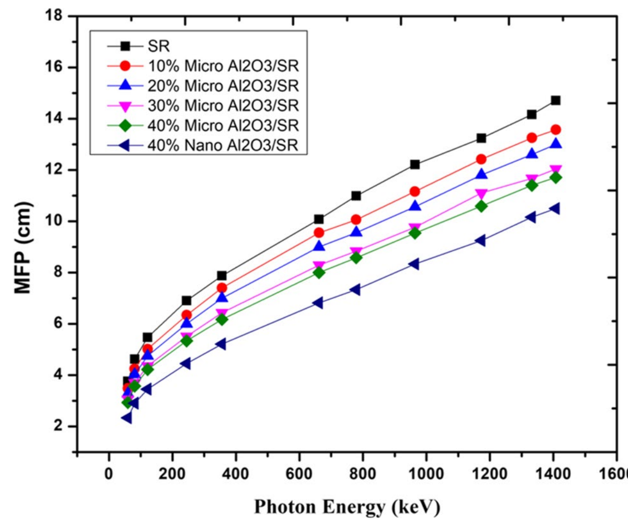

Fig. 12 The variation of the mean free path as a function of photon energy

in comparison to their micro counterparts, as will be seen in the next figures.

Figure 9 illustrates the changes in the linear attenuation coefficient (LAC) of free silicone rubber, as well as (10%, 20%, 30%, 40%) micro Al_2O_3/SR and 40% nano Al_2O_3/SR composites. The LAC increases with an increase in the concentration of bulk aluminum oxide. Furthermore, the LAC values for nano-sized composites are higher compared to those of micro-sized composites. This observation aligns with the density-dependent nature of LAC, where an increase in density leads to a corresponding increase in LAC.

To explore the shielding capabilities of current composites against gamma rays, we have calculated several parameters based on Linear attenuation coefficient (LAC). These parameters include the half value layer (HVL), the tenth value layer (TVL), and the mean free path (MFP). It is worth noting that lower values of these parameters indicate better shielding performance.

In Figs. 10, 11, and 12, we present the variations in HVL, TVL, and MFP values across all samples, considering the incident photon energy. These figures demonstrate that these parameters are dependent on photon energy. As the incident photon energy increases, we observe a corresponding increase in HVL, TVL, and MFP values. This implies that higher energy photons have a reduced likelihood of interacting with the sample, thereby allowing for enhanced photon penetration. Figure 13 illustrates the relationship between energy and

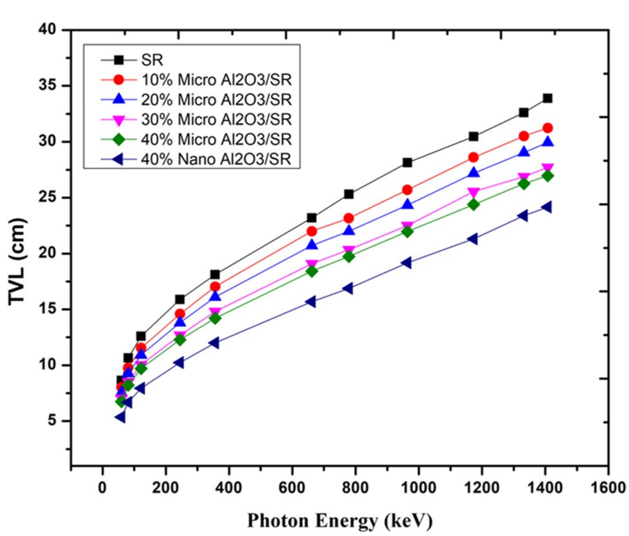

Fig. 11 The variation of the TVL as a function of photon energy

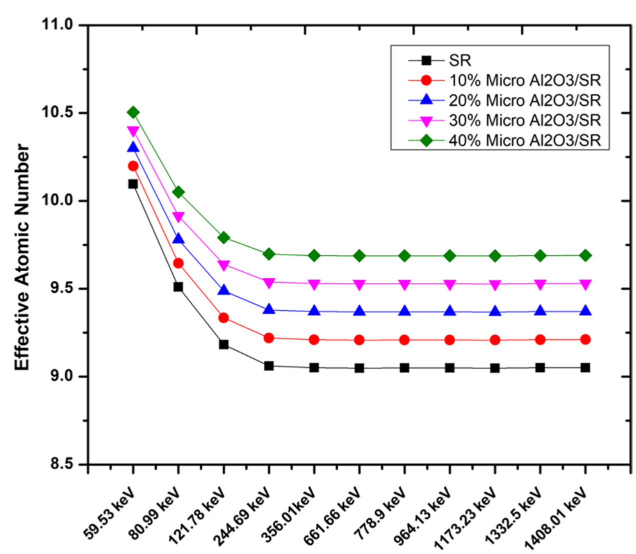

Fig. 13 The effective atomic number of free silicone rubber, 10%,20%,30%, and 40% Al_2O_3/SR for different gamma-ray energies

Table 5 The ratio of HVL value of Al_2O_3/SR composites to HVL of 40% Micro Pb/SR

Energy (keV)	HVL			HVL composite / HVL 40% Micro Pb/SR	
	40% Micro Al_2O_3/SR	40% Nano Al_2O_3/SR	40% Micro Pb/SR (XCOM)	40% Micro Al_2O_3/SR	40% Nano Al_2O_3/SR
59.51	2.029	1.616	0.194	10.463	8.334
80.99	2.472	2.011	0.415	5.958	4.849
121.78	2.923	2.393	0.278	10.520	8.613
244.7	3.695	3.084	1.254	2.948	2.460
356.01	4.278	3.612	2.255	1.897	1.602
661.66	5.545	4.724	4.215	1.315	1.121
778.9	5.945	5.080	4.756	1.250	1.068
964.08	6.614	5.775	5.499	1.203	1.050
1173.24	7.343	6.414	6.223	1.180	1.031
1332.5	7.906	7.041	6.704	1.179	1.050
1408.01	8.119	7.275	6.909	1.175	1.053

the variation of effective atomic number. It demonstrates that as energy increases, the effective atomic number decreases, which is dependent on the mass attenuation coefficient. Additionally, an increase in aluminum oxide concentration leads to higher values of the effective atomic number.

Table 5 presents the ratio of the half value layer (HVL) of composites containing 40% Micro Al_2O_3/SR and 40% Nano Al_2O_3/SR to the HVL of pure 40% Micro Pb/SR. This assessment aims to determine the effectiveness of these composites as shielding materials. At an energy level of 59.51 keV, it is evident that a thickness of 2.029 cm of 40% Micro Al_2O_3/SR is equivalent to 0.194 cm of 40% Micro Pb/SR shield. This means that the 40% Micro Al_2O_3/SR composite is 10.463 times thicker than the 40% Micro Pb/SR shield. On the other hand, at an energy level of 1408.1 keV, a thickness of 8.119 cm of 40% Micro Al_2O_3/SR is similar to 6.909 cm of 40% Micro Pb/SR. In this case, the 40% Micro Al_2O_3/SR composite is only 1.175 times thicker than the 40% Micro Pb/SR shield. Furthermore, it is evident that a thickness of 1.616 cm of 40% Nano Al_2O_3/SR is equivalent to 0.194 cm of 40% Micro Pb/SR shield at 59.51 keV. This indicates that the 40% Nano Al_2O_3/SR composite is 8.334 times thicker than the 40% Micro Pb/SR shield. Similarly, at an energy level of 1408.1 keV, a thickness of 7.275 cm of 40% Nano Al_2O_3/SR is similar to 6.909 cm.

Table 6 Comparison of the LAC between our result and 20% Micro and Nano SnO_2/SR [10] at different energies

Energy (keV)	Linear attenuation coefficient, cm^{-1}			
	40% Micro Al_2O_3/SR	20% Micro SnO_2/SR [10]	40% Nano Al_2O_3/SR	20% NanoSnO_2/SR [10]
59.51	0.342	1.632	0.429	2.072
80.99	0.280	0.847	0.345	1.09
121.78	0.237	0.386	0.290	0.488
244.7	0.188	0.192	0.225	0.241
356.01	0.162	0.152	0.192	0.188
661.66	0.125	0.115	0.147	0.139
778.9	0.117	0.104	0.136	0.12
964.08	0.105	0.094	0.120	0.106
1173.24	0.094	0.085	0.108	0.096
1332.5	0.088	0.079	0.098	0.088
1408.01	0.085	0.077	0.095	0.085

Table 6 represents a comparison of the linear attenuation coefficient at different gamma ray energies between the data explained in Gouda M. M. et al. [10] where silicon rubber is reinforced with 20% micro- and nanotin oxide. The comparison described that LAC of 20% tin oxide was higher than 40% aluminum oxide at low energies, but as the energy increased, the values of 40% micro- and nano- Al_2O_3/SR became higher than the values of 20% micro and nano tin oxide, and that is according to increasing the density of the composite. This led to the validity of using light elements as filler in the composite, but with high concentrations to get acceptable results.

4 Conclusion

To examine the capability of radiation attenuation, aluminum nanoparticles were produced in this study using the electric arc discharge method. The effect of particle size on radiation shielding capabilities is studied using micro- and nano-sized aluminum nanoparticles. With photon energies ranging from 59.53 keV to 1408 keV, the shielding properties of the composites were measured using a NaI scintillation detector. According to the SEM and TEM images that were taken of the generated samples, the addition of nanoparticles and nanowires improved the morphological and homogenous qualities more than the inclusion of microparticles. The results show that there is good agreement between the theoretical values acquired from the XCOM program and the experimental values of the MACs for bulk samples. The results show that nano aluminum oxide composites have superior gamma ray shielding properties in comparison to micro aluminum oxide composites. Also, increasing the weight percentage of aluminum oxide led to an increase in density, which proved that, when it comes to radiation protection, aluminum oxide with a high concentration has a better linear attenuation coefficient.

Author Contributions E.M.S., A.M.E. and M.M.G. wrote the main manuscript text, A.M.E. and M.S.H. prepared Figures. A.M.E. and E.E revised the tables and figures. All authors reviewed the manuscript.

Funding Open access funding provided by The Science, Technology & Innovation Funding Authority (STDF) in cooperation with The Egyptian Knowledge Bank (EKB). The authors declare that no funds, grants, or other support were received during the preparation of this manuscript.

Data Availability All data generated or analyzed during this study are included in this published article.

Declarations

Ethics Approval Not applicable.

Consent to Participate Not applicable.

Consent for Publication Not applicable.

Competing Interests The authors declare no competing interests.

References

1. Attix FH (2008) Introduction to radiological physics and radiation dosimetry. John Wiley & Sons. https://doi.org/10.1002/9783527617135
2. Badawi MS (2009) Comparative Study of the Efficiency of Gamma-rays Measured by 190 Compact-and Well Type-Cylindrical Detectors. PhD Thesis, Alexandria University, Egypt. https://doi.org/10.1016/j.apradiso.2012.12.011
3. El-Khatib AM et al (2022) Assessment of γ-radiation shielding behavior of some mixed nature clays. Radiat. Radiat Phys. Chem. https://doi.org/10.1016/j.radphyschem.2022.110236
4. Ahmed M, El-Khatib MM, Gouda MS, Fouad M, Abd-Elzaher, Ramadan W (2023) Radiation attenuation properties of chemically prepared MgO nanoparticles/HDPE composites. Sci Rep 13:1. https://doi.org/10.1038/s41598-023-37088-y
5. Elsafi M et al (2022) Effect of iron and ferrosilicon materials to enhance the radiation shielding ability of bentonite clay. Radiation Physics and Chemistry. https://doi.org/10.1016/j.radphyschem.2022.110235
6. Abbas YM, El-Khatib AM, Mohamed SB, Mahmoud TA and Osama MH (2021) 'GAMMA ATTEN UATION THROUGH NANO LEAD – NANO COP PER PVC COM POS ITES', doiSerbia, 36:50–59. https://doi.org/10.2298/NTRP210110001A
7. KN Sridhar, L Seenappa, HC Manjunatha, YS Vidya, BC Reddy, S Manjunatha, AN Santhosh, R Munirathnam, AC Raj, PSD Gupta, BM Sankarshan, KV Sathish (2023) 'X-ray/gamma radiation shielding properties of Aluminium-BariumZinc Oxide nanoparticles synthesized via low temperature solution combustion method', Nuclear Engineering and Technology, Feb. https://doi.org/10.1016/j.apradiso.2018.05.014
8. Kaur S, Singh KJ (2014) 'Investigation of lead borate glasses doped with aluminium oxide as gamma ray shielding materials', Ann Nucl Energy, Jan. https://doi.org/10.1016/j.anucene.2013.08.012
9. El-khatib AM, Abbas MI, Saleh M, Hassanien HS, Kashyout AEH, 'Nano Iron loaded polymeric composite as gamma radiation shielding application. https://doi.org/10.1038/s41598-023-40846-7
10. Gouda MM, Abbas AM, Hammoury SI, Zard K, El-Khatib AM (2023) 'Nano tin oxide/dimethyl polysiloxane reinforced composite as a flexible radiation protecting material', Sci. Rep. https://doi.org/10.1038/s41598-023-27464-z
11. Lin ZI et al (2017) Conductive fabrics made of polypropylene/multi-walled carbon nanotube coated polyester yarns: Mechanical properties and electromagnetic interference shielding effectiveness. Sci Technol 141:74–82. https://doi.org/10.1016/j.compscitech.2017.01.013
12. Ray SS, Okamoto M (2003) 'Polymer/layered silicate nanocomposites: a review from preparation to processing', pp. 1539–1641. https://doi.org/10.1016/j.progpolymsci.2003.08.002
13. Hosseini MA, Malekie S, Kazemi (2022) 'Experimental evaluation of gamma radiation shielding characteristics of Polyvinyl Alcohol/Tungsten oxide composite: A comparison study of micro and nano sizes of the fillers', Nucl Instrum Methods Phys Res A, Mar. https://doi.org/10.1016/j.nima.2021.166214
14. Malekie S, Kashian S, Akhavan A, Kheradmand-Saadi M (2023) 'Preliminary study of a novel radiation shield for jaw in dental radiography using the high-density polyethylene/bismuth oxide nanocomposite', Radiation Physics and Chemistry, Apr. https://doi.org/10.1016/j.radphyschem.2022.110743
15. El-Khatib MA, Abbas AM, Hammoury SI, Gouda MM, Zard K, Elsafi M (2022) 'Effect of PbO-Nanoparticles on Dimethyl Polysiloxane for use in Radiation Shielding Applications', Sci. Rep. 12. https://doi.org/10.1038/s41598-022-20103-z
16. Mehrara R, Malekie S, Kotahi SMS, Kashian S (2021) Introducing a novel low energy gamma ray shield utilizing Polycarbonate Bismuth Oxide composite. Sci Rep 11:10614. https://doi.org/10.1038/s41598-021-89773-5
17. Malekie S, Shooli H, Hosseini MA (2022) 'Assessment of new composites containing polyamide-6 and lead monoxide as shields against ionizing photonic radiation based on computational and experimental methods', Scientific Reports volume, pp. 1–15. https://doi.org/10.1038/s41598-022-13556-9
18. Mirji R, Lobo B, (2017) ' "Radiation shielding materials: A brief review on methods, scope and significance," P. C. Jabin Science College, Huballi, Karnataka, India, Volume: JAB-INTRONICS-2017, ISBN 978-81-931806-8-6; Pages 96–100
19. Baibarac M, Gómez-Romero P (2016) Nanocomposites Based on Conducting Polymers and Carbon Nanotubes from Fancy Materials to Functional Applications. J Nanosci Nanotechnol 6:1–14. https://doi.org/10.1166/jnn.2006.002
20. Alabsy MT, Gouda MM, Abbas MI, Al-Balawi SM, El-Khatib AM (2023) 'Enhancing the Gamma-Radiation-Shielding Properties of Gypsum–Lime–Waste Marble Mortars by Incorporating Microand Nano-PbO Particles', Materials. https://doi.org/10.3390/ma16041577
21. Shen H et al (2023) ' The effect of modified carbon-doped boron nitride on the mechanical, thermal and γ-radiation stability of silicone rubber composites ', Polymer Degradation and Stability, 218 110524. https://doi.org/10.1016/j.polymdegradstab.2023.110542

22. Rammah YS, Kumar A, Mahmoud KAA, El-Mallawany R, El-Agawany FI, Tekin HO, Susoy G, (2020) 'SnO Reinforced Silicate Glasses and Utilization in Gamma Radiation Shielding Applications. ', Emerging Materials Research, 9 3:1–8. https://doi.org/10.1680/jemmr.20.00150
23. Tavacoli-Anbaran H, Alavian H (2019) Study on gamma shielding polymer composites reinforced with different sizes and proportions of tungsten particles using MCNP code. Prog Nucl Energy 115:91–98. https://doi.org/10.1016/j.pnucene.2019.03.033
24. Wang J, Zhao D, Zhou G, Zhang C, Zhang P, Hou X (2020) 'Synthesis of nano-sized γ-Al2O3 with controllable size by simple homogeneous precipitation method', ELSEVIER. https://doi.org/10.1016/j.matlet.2020.128476
25. Bell TE, González-Carballo JM, Tooze RP, Torrente-Murciano L 'Single-step synthesis of nanostructured γ-alumina with solvent reusability to maximise yield and morphological purity', J Mater Chem A Mater, pp. 6196–6201. https://doi.org/10.1039/C4TA06692H
26. Hun-Sik K, Soon-Min K, Kwang HL, Jin-San Y, Hyoung-Joon J (2008) ' Preparation and characterization of silicone rubber/functionalized carbon nanotubes composites via in situ polymerization. ', J. Nanosci. Nanotechnol., vol. 8, no. 10, pp. 5551–5554. https://doi.org/10.1166/jnn.2008.1312
27. Gouda MM, Badawi MS, El-Khatib AM, Hussien NS, Abbas MI 2016 "Calculation of Nal(Tl) detector full-energy peak efficiency using the efficiency transfer method for small radioactive cylindrical sources", Nuclear Technology and Radiation Protection, 31 2 150–158. https://doi.org/10.2298/NTRP1602150G
28. Gouda MM (2019) "Calibration of NaI (Tl) Cylindrical Detector Using Axially Shifted Radioactive Cylindrical Sources." Nucl Technol Radiat Prot 34:353–360
29. Badawi MS, El-Khatib AM, Gouda MM (2016) '"New numerical simulation method to calibrate the regular hexagonal NaI(Tl) detector with radioactive point sources situated non-axial" ', Review of Scientific Instruments, 87 11:115105
30. Abbas MI et al (2021) NaI cubic detector full-energy peak efciency, including coincidence and self-absorption corrections for rectangular sources using analytical method. J. Radioanal. Nucl Chem 327:251–258. https://doi.org/10.1007/s10967-020-07508-8
31. Badawi MS et al (2017) "Calibration of 4π NaI(Tl) detectors with coincidence summing correction using new numerical procedure and ANGLE4 software." AIP Adv 7(3):035005. https://doi.org/10.1063/1.4978214
32. El-Khatib AM, Gouda MM, Badawi MS, Nafee SS, El-Mallah EA (2013) "Computation of the full energy peak efficiency of an hpge detector using a new compact simulation analytical approach for spherical sources." J Eng Sci Technol 8(5):623–638. https://doi.org/10.1016/j.jestch.2013.10.001
33. Abbas MI et al (2021) NaI cubic detector full-energy peak efficiency, including coincidence and self-absorption corrections for rectangular sources using analytical method. J Radioanal Nucl Chem 327(1):251–258. https://doi.org/10.1007/s10967-020-07508-8
34. El-Khatib AM et al (2016) Well-type NaI(Tl) detector efficiency using analytical technique and ANGLE 4 software based on radioactive point sources located out the well cavity. Chin J Phys 54(3):338–346. https://doi.org/10.1016/j.cjph.2016.03.019
35. Gouda MM, Obeid A, Awad R, Badawi MS (2023) Gamma-ray attenuation parameters of HDPE filled with different nano-size and Bulk WO3. Appl Rad Isot 197:110790
36. 'https://physics.nist.gov/PhysRefData/Xcom/html/xcom1.html'
37. Shoag JM, Burns KM, Kahlon SS, Parsons PJ, Bijur PE, Taragin BH, Markowitz M (2020) Lead poisoning risk assessment of radiology workers using lead shields. Arch. Environ. Occup. Health. Environ Occup Health 60–64. https://doi.org/10.1080/19338244.2018.1553843
38. Alım B (2020) comprehensive study on radiation shielding characteristics of Tin-Silver, Manganin-R, Hastelloy-B, Hastelloy-X and Dilver-P alloys. Appl Phys 126(4):1–19. https://doi.org/10.1007/s00339-020-3442-7
39. Ara A, Usmani JA (2015) Lead toxicity: A review. Interdiscip. Toxicol. J A Lead toxicity 55–64. https://doi.org/10.1515/intox-2015-0009
40. Schlattl H, Zankl M, Hoeschen C, Eder H (2007) Shielding properties of lead-free protective clothing and their impact on radiation doses. Med Phys 34(11):4270–4280. https://doi.org/10.1118/1.2786861
41. Abbas MI et al (2023) Investigation of Gamma-Ray Shielding Properties of Bismuth Oxide Nanoparticles with a Bentonite–Gypsum Matrix. Materials 16:2056. https://doi.org/10.3390/ma16052056
42. Zhang Y, Li R, Zhou X, Cai M, Sun X (2008) 'Selective Growth of α-Al2O3 Nanowires and Nanobelts', Hindawi Publishing Corporation Journal of Nanomaterials. https://doi.org/10.1155/2008/250370
43. Li WF, Ma XL, Zhang WS, Li Y, Zhang ZD (2006) 'Synthesis and characterization of γ-Al2O3 nanorods', WILEY, 294–299. https://doi.org/10.1039/C9MH01371G
44. Lin PC, Lin S, Wang PC, Sridhar R (2014) Techniques for physicochemical characterization of nanomaterials. 711–726. https://doi.org/10.1016/j.biotechadv.2013.11.006
45. Mourdikoudis S, Pallares RM, Thanh NTK (2018) 'Characterization techniques for nanoparticles:comparison and complementarity upon studyingnanoparticle properties', https://doi.org/10.1039/C8NR02278J
46. Zou H, Wu S, Shen J (2008) 'Nanocomposites: Preparation, Characterization, Properties, and Applications, 3893–3957 https://doi.org/10.1155/2018/4749501
47. Vatankhah AR , Hosseini MA, Malekie S (2019) The characterization of gamma-irradiated carbon-nanostructured materials carried out using a multi-analytical approach including Raman spectroscopy. Appl Surf Sci 671–680. https://doi.org/10.1016/j.apsusc.2019.05.294
48. Ebrahimi N, Hosseini MA, Malekie S (2020) Preliminary study of linearity response of γ-irradiated graphene oxide as a novel dosimeter using the Raman spectroscopy. Bullet Materials Science 43:1–5. https://doi.org/10.1007/s12034-020-02177-5
49. Ebrahimi N, Hosseini MA, Malekie S (2020) Preliminary study of linearity response of γ-irradiated graphene oxide as a novel dosimeter using the Raman spectroscopy. Bullet Mat Sci 43:1–5. https://doi.org/10.1007/s12034-020-02177-5